

Wafer-Scale Patterning Integration of Chiral 3D Perovskite Single Crystals toward High-Performance Full-Stokes Polarimeter

Junli Bai,[▽] Hebin Wang,[▽] Jianpeng Ma, Yingjie Zhao,* Haolin Lu, Yunxin Zhang, Sehrish Gull, Tianjiao Qiao, Wei Qin, Yongsheng Chen, Lei Jiang, Guankui Long,* and Yuchen Wu*



Cite This: *J. Am. Chem. Soc.* 2024, 146, 18771–18780



Read Online

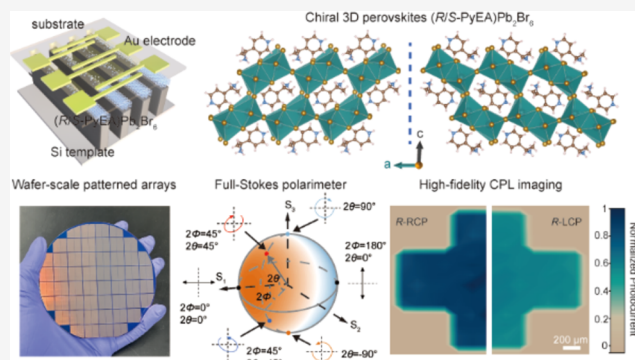
ACCESS |

Metrics & More

Article Recommendations

Supporting Information

ABSTRACT: Chiral three-dimensional (3D) perovskites exhibit exceptional optoelectronic characteristics and inherent chiroptical activity, which may overcome the limitations of low-dimensional chiral optoelectronic devices and achieve superior performance. The integrated chip of high-performance arbitrary polarized light detection is one of the aims of chiral optoelectronic devices and may be achieved by chiral 3D perovskites. Herein, we first fabricate the wafer-scale integrated full-Stokes polarimeter by the synergy of unprecedented chiral 3D perovskites (*R/S*-PyEA)Pb₂Br₆ and one-step capillary-bridge assembly technology. Compared with the chiral low-dimensional perovskites, chiral 3D perovskites present smaller exciton binding energies of 57.3 meV and excellent circular dichroism (CD) absorption properties, yielding excellent circularly polarized light (CPL) photodetectors with an ultrahigh responsivity of 86.7 A W⁻¹, an unprecedented detectivity exceeding 4.84 × 10¹³ Jones, a high anisotropy factor of 0.42, and high-fidelity CPL imaging with 256 pixels. Moreover, the anisotropic crystal structure also enables chiral 3D perovskites to have a large linear-polarization response with a polarized ratio of 1.52. The combination of linear-polarization and circular-polarization discrimination capabilities guarantees the achievement of a full-Stokes polarimeter. Our study provides new research insights for the large-scale patterning wafer integration of high-performance chiroptical devices.



INTRODUCTION

Hybrid organic–inorganic metal halide perovskites gain substantial attention due to the large absorption coefficients, tunable band gaps, high carrier mobility, long carrier diffusion lengths, and low-cost solution processing, which greatly accelerate the development of solar cells,^{1–3} light-emitting diodes,^{4–6} photodetectors,^{7–9} and lasers.^{10–12} In particular, the construction of chiral perovskites yields numerous exotic properties, including circular dichroism (CD),^{13,14} nonlinear chiroptical properties,^{15,16} ferroelectricity,^{17,18} and chirality-induced spin selectivity (CISS) effect,^{19,20} which significantly broadens the applications of perovskites in various fields including circularly polarized light (CPL) photodetectors,^{21,22} nonlinear optics,²³ memories,²⁴ and spin-LEDs.²⁵ The current fabrication of chiral perovskite optoelectronic devices is usually based on the chiral low-dimensional perovskite materials, such as (*R/S*- α -PEA)PbI₃,²⁶ (*R/S*- α -PEA)₂PbI₄,²⁷ (*R/S*- β -MPA)₂MAPb₂I₇,²⁸ and (*R/S*-BPEA)₂PbI₄.²⁹ These devices expose some intrinsic limitations, such as poor charge carrier mobility, low responsivity, and small anisotropy factor. The manufacturing of chiral three-dimensional (3D) perovskites represents a promising approach to address these limitations and achieve superior performance in chiral optoelectronic

devices, but the incorporation of large chiral cations typically breaks down the structure of chiral 3D perovskite due to an undesirable structure tolerance factor.^{30,31} Furthermore, thermodynamically stabilized chiral 3D perovskites have been predicted by theoretical calculations, but they have not been explored experimentally.³² Therefore, it is absolutely necessary to design appropriate A-site chiral cations, which will be helpful in composing stable chiral 3D perovskites for the advancement of chiral optoelectronic devices.

The performance of perovskite devices greatly relies on the crystallization quality and orientation of the perovskite crystals along with optoelectronic features such as carrier mobility and exciton binding energy.^{33,34} To fabricate long-range ordered perovskite crystals, numerous methods such as hot casting,³⁵ composition engineering,³⁶ solvent engineering,³⁷ and surface modification³⁸ have been developed, which effectively reduce

Received: May 19, 2024

Revised: June 10, 2024

Accepted: June 17, 2024

Published: June 27, 2024



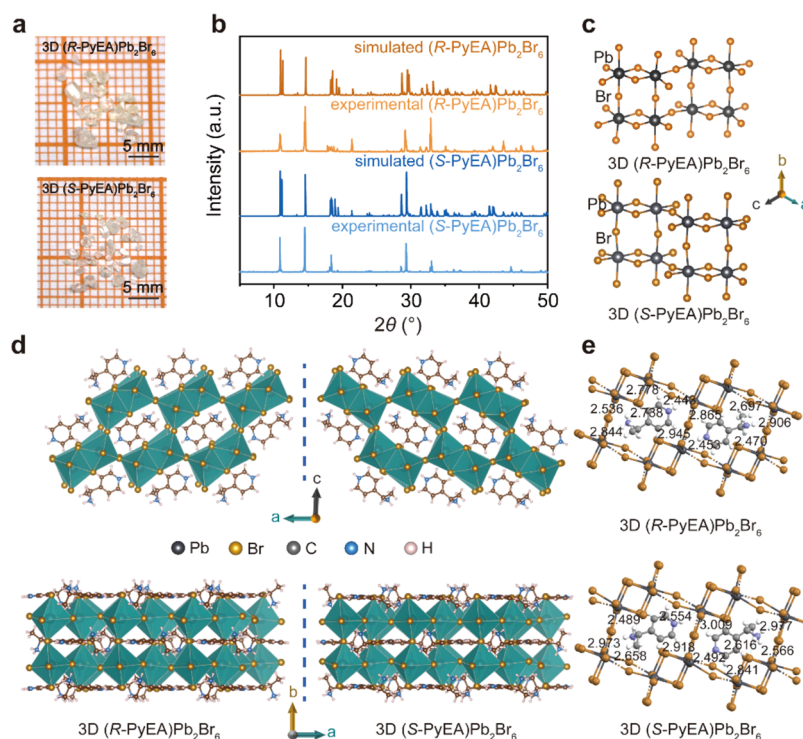


Figure 1. Crystal structure characterization of $(R\text{-PyEA})\text{Pb}_2\text{Br}_6$ and $(S\text{-PyEA})\text{Pb}_2\text{Br}_6$ perovskite single crystals. (a) Photographs of $(R\text{-PyEA})\text{Pb}_2\text{Br}_6$ and $(S\text{-PyEA})\text{Pb}_2\text{Br}_6$ perovskite single crystals, respectively. (b) Simulated and experimental powder XRD patterns of $(R\text{-PyEA})\text{Pb}_2\text{Br}_6$ and $(S\text{-PyEA})\text{Pb}_2\text{Br}_6$ perovskite single crystals. (c) Fragment of $(R\text{-PyEA})\text{Pb}_2\text{Br}_6$ and $(S\text{-PyEA})\text{Pb}_2\text{Br}_6$ perovskite structure exhibiting the coordination environment of octahedra. (d) A schematic illustration of the chiral 3D perovskite structure of $(R\text{-PyEA})\text{Pb}_2\text{Br}_6$ and $(S\text{-PyEA})\text{Pb}_2\text{Br}_6$ perovskites, possessing distinct mirror symmetry. (e) Asymmetric hydrogen bonding interactions between the Br atoms and PyEA^{2+} cations in $(R\text{-PyEA})\text{Pb}_2\text{Br}_6$ and $(S\text{-PyEA})\text{Pb}_2\text{Br}_6$ perovskites.

grain boundaries and defects in perovskite films. To further improve the performance of optoelectronic devices, perovskite single-crystal films with long-range orientation need to be stringently controlled.^{39–41} In this sense, integrated perovskite micro/nano single-crystal microwire arrays with pure crystallographic orientation are necessary to meet the miniaturization and integration of optoelectronic devices.⁴² However, the current integration technology faces issues such as poor crystal quality, complicated processing, and small arrayed areas. Therefore, the development of a cost-effective, large-area, single-crystal, and long-range oriented perovskite microwire array technology is strongly needed for high-performance detection and imaging.

In this study, we reported a novel chiral 3D perovskite, $(R/S\text{-PyEA})\text{Pb}_2\text{Br}_6$, through rational design of the chiral cations, and then fabricated the integrated CPL photodetectors based on the chiral 3D perovskites by a one-step capillary-bridge assembly technology. Owing to the hydrogen bonding interactions between the chiral ammonium cations and octahedral units, the chiral 3D perovskites $(R/S\text{-PyEA})\text{Pb}_2\text{Br}_6$ with a combination of corner- and edge-sharing octahedral units exhibit excellent structural stability. Owing to excellent CD, single crystallinity, and pure crystallographic orientation of the chiral 3D perovskite microwire arrays, CPL photodetector exhibits a superior responsivity of 86.7 A W^{-1} , a detectivity exceeding 4.84×10^{13} Jones, a circular-polarization/linear-polarization anisotropy factor of 0.42/1.52, and large-area high-fidelity imaging with 256 pixels. By the synergy of excellent CPL discrimination performance and large linear-polarization capability, a full-Stokes polarimeter was eventually demonstrated. Our study provides a new route for low-cost

and large-area patterning of integrated chiral optoelectronic devices.

RESULTS AND DISCUSSION

3D perovskites are a class of periodically repeating structures consisting of lead-halide octahedral units in the direction of three spatial axes, presenting superior optoelectronic features and isotropic carrier transport properties. Inspired by the previous work of achiral 3D perovskites,⁴³ we introduce (R/S) -1-(pyridine-4-yl)ethan-1-amine ($R/S\text{-PyEA}$) as chiral cations and construct the chiral 3D perovskite $(R/S\text{-PyEA})\text{Pb}_2\text{Br}_6$ crystals with the maximum size of $3 \times 2 \times 1 \text{ mm}^3$ via a simple solution diffusion crystallization method (Figure 1a). The detailed synthesis method is shown in the Experimental Section. The powder X-ray diffraction (XRD) patterns of $(R/S\text{-PyEA})\text{Pb}_2\text{Br}_6$ perovskite crystals are in good agreement with the simulated results, demonstrating their phase purity (Figure 1b). The single-crystal diffraction analysis of $(R/S\text{-PyEA})\text{Pb}_2\text{Br}_6$ perovskites presents a monoclinic structure with the $P2_1$ Sohncke space group, with cell parameters of $a = 9.2839(2) \text{ \AA}$, $b = 12.0954(3) \text{ \AA}$, $c = 16.1719(4) \text{ \AA}$, $\alpha = 90.0000^\circ$, $\beta = 93.315(2)^\circ$, $\gamma = 90.0000^\circ$, and $V = 1812.94(7) \text{ \AA}^3$, respectively (see details in Table S1). The low symmetry of chiral 3D perovskite monoclinic crystals leads to the anisotropic crystal structure and thus allows for the discrimination of linearly polarized light.⁴⁴ The basic units in chiral 3D perovskites consist of two edge-sharing PbBr_6 octahedra, which are connected by corner-sharing in three dimensions to form the 3D inorganic framework (Figure 1c). Upon introduction of chiral cations, $(R\text{-PyEA})\text{Pb}_2\text{Br}_6$ and $(S\text{-PyEA})\text{Pb}_2\text{Br}_6$

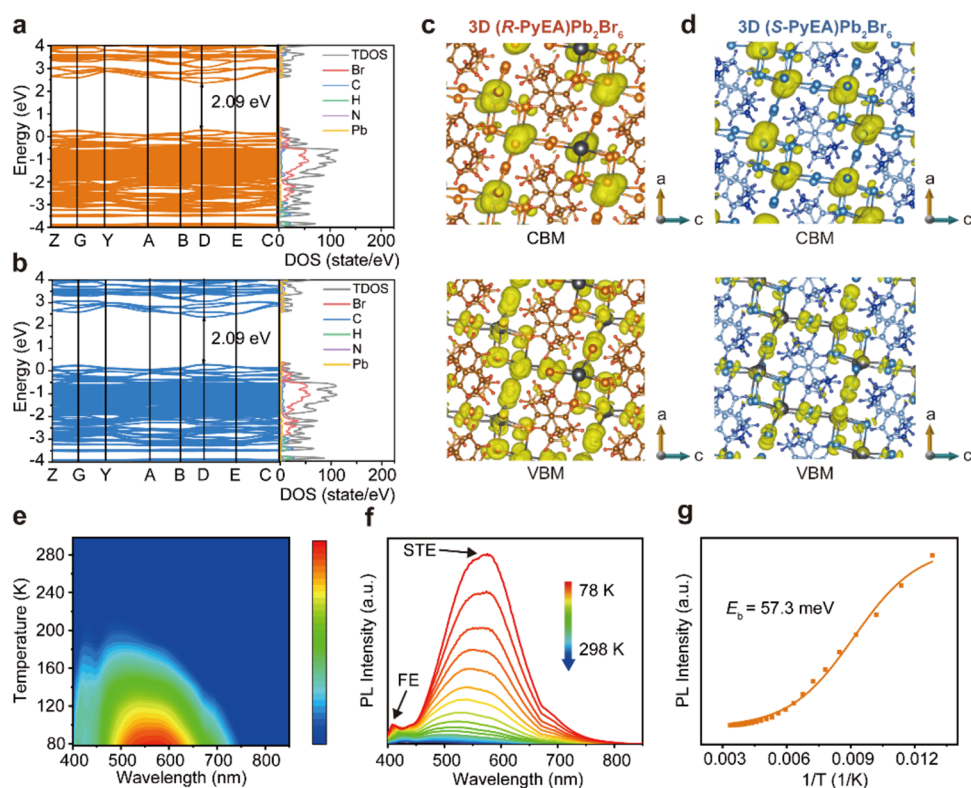


Figure 2. Intrinsic energy band structure and exciton binding energy of chiral 3D perovskites. (a, b) Calculated electronic band structures and partial density of states of (R-PyEA)Pb₂Br₆ perovskite (a) and (S-PyEA)Pb₂Br₆ perovskite (b). (c, d) Isosurface plots of the wave functions of VBM and CBM of (R-PyEA)Pb₂Br₆ perovskite (c) and (S-PyEA)Pb₂Br₆ perovskite (d). (e, f) Temperature-dependent photoluminescence spectra of (R-PyEA)Pb₂Br₆ perovskites. (g) The exciton binding energy of (R-PyEA)Pb₂Br₆ perovskites fitted by the Arrhenius formula.

PyEA)Pb₂Br₆ perovskites show a distinct mirror symmetry structure (Figures 1d and S1). Meanwhile, each S-PyEA chiral cation presents hydrogen bonding interactions (N–H···Br and C–H···Br) with the inorganic framework as shown in Figure 1e. These hydrogen bonds have asymmetric interactions with Br atoms owing to each Br atom forming a different type of hydrogen bond (Figure S2 and Table S2). The hydrogen bonds in (S-PyEA)Pb₂Br₆ range from 2.453 to 2.984 Å, which are similar to those in the (R-PyEA)Pb₂Br₆ perovskite. The Hirshfeld surfaces and two-dimensional (2D)-fingerprint plots of the 3D chiral perovskites indicate that hydrogen bonding interactions contribute 88.7 and 89.2% between organic molecules and inorganic frameworks in (R-PyEA)Pb₂Br₆ and (S-PyEA)Pb₂Br₆ perovskites (Figure S3). Therefore, the stabilized structure of chiral 3D perovskites should be attributed to the hydrogen bonding interactions between the large chiral ammoniums and the inorganic framework. Thermogravimetric tests further demonstrate excellent structural stability of the chiral 3D perovskites (Figure S4).

To further investigate the intrinsic energy band structure and the exciton binding energy of (R-PyEA)Pb₂Br₆ and (S-PyEA)Pb₂Br₆ perovskites, density functional theory (DFT) calculations and temperature-dependent photoluminescence tests were carried out. As shown in Figure 2a,b, (R-PyEA)Pb₂Br₆ and (S-PyEA)Pb₂Br₆ perovskites present direct band gap characteristics due to both the valence band maximum (VBM) and the conduction band minimum (CBM) being located at the same D point. Direct band gap semiconductors ensure strong optical absorption.⁴⁵ The partial density of states (DOS) around the Fermi level reveals that the inorganic octahedra framework within the (R-PyEA)Pb₂Br₆

and (S-PyEA)Pb₂Br₆ perovskites makes a dominant contribution to the energy band gap. To obtain the band gap of chiral 3D perovskite, the solid-state diffuse reflectance spectrum (DRS) was carried out. As shown in Figure S5, experimental band gaps of (R-PyEA)Pb₂Br₆ and (S-PyEA)Pb₂Br₆ perovskites are about 2.98 eV (416 nm) and 2.95 eV (420 nm), respectively. Compared with the experimental band gap, the calculated band gap has a reasonable expected decrease due to the underestimate based on the PBE function.⁴⁶ In addition, the isosurface plots of the wave functions of VBM and CBM also demonstrate that the charge density is predominantly distributed on the PbBr₆ octahedra (Figure 2c,d). More importantly, the isosurface plots of the wave functions of CBM and VBM also exhibit an electronic 3D feature. To further demonstrate the isotropic carrier transport ability, the effective masses of chiral 3D perovskites were further estimated according to the definition

$$\frac{1}{m^*} = \frac{1}{\hbar} \frac{d^2 E(k)}{d^2 k}$$

where m^* is the effective mass, $E(k)$ is the energy of a band, and k is the wave vector. As shown in Table S3, the electron and hole effective masses of the (R/S-PyEA)Pb₂Br₆ perovskite are of the same magnitude along three directions, demonstrating the 3D carrier transport feature. The performance of perovskite optoelectronic devices greatly depends on carrier generation and transport, and small exciton binding energies can effectively enhance the performance of optoelectronic devices.⁴⁷ To prove that chiral 3D perovskites possess a smaller exciton binding energy, we quantitatively extracted the exciton

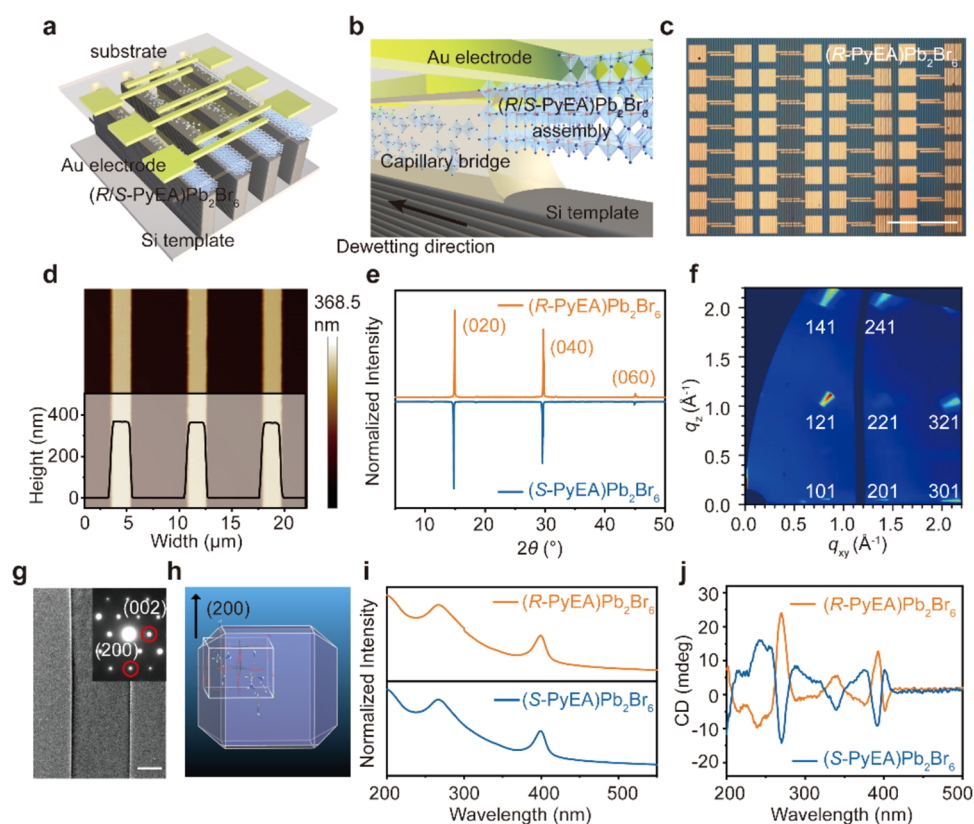


Figure 3. Morphology, crystallinity, and optical properties of chiral 3D perovskite microwire arrays. (a, b) A schematic illustration of the fabrication process of chiral 3D perovskite microwire arrays. (c) Optical microscope image of (R-PyEA)Pb₂Br₆ perovskite microwire arrays. (d) Atomic force microscopy (AFM) image of three adjacent (R-PyEA)Pb₂Br₆ perovskite microwires. (e) XRD pattern of (R-PyEA)Pb₂Br₆ and (S-PyEA)Pb₂Br₆ perovskite microwire arrays. (f) Grazing-incidence wide-angle X-ray scattering (GIWAXS) pattern of (R-PyEA)Pb₂Br₆ microwire arrays. The sharp diffraction spots indicate high crystallinity and pure (200) crystallographic orientation. (g) Transmission electron microscopy (TEM) image and selected area electron diffraction (SAED) pattern of single-crystalline microwire arrays of (R-PyEA)Pb₂Br₆ perovskite. (h) Simulated Bravais–Friedel–Donnay–Harker (BFDH) morphology of (R-PyEA)Pb₂Br₆ perovskite crystals. (i) Absorbance spectra and (j) CD spectra of (R-PyEA)Pb₂Br₆ and (S-PyEA)Pb₂Br₆ perovskite microwire arrays. Scale bars: (c) 200 μm; (g) 1 μm.

binding energy of (R-PyEA)Pb₂Br₆ perovskites by measuring temperature-dependent photoluminescence. As increasing temperature from 78 to 298 K, the photoluminescence intensity of chiral 3D perovskites decreases gradually, accompanied by a broadening of the photoluminescence spectrum (Figure 2e). The two PL peaks observed in the temperature-dependent photoluminescence spectrum can be assigned as free exciton (FE) and self-trapped exciton (STE) emission.^{48–50} At high temperatures, the STE emission is suppressed, which is a typical characteristic of STE due to thermal dissociation and thus more FE emission. At 78 K (low thermal activation), most of the excitons are self-trapped, resulting in a strongly Stokes-shifted broadband luminescence. In addition, the FE peak exhibits a red shift with the temperature increasing, owing to the temperature-induced lattice expansion leading to the shift in the relative position of the conduction and valence bands.⁵¹ A noticeable blue shift of STE peak is also observed as the temperature increases, which should be attributed to a stabilization of out-of-phase band-edge states as the lattice expands.⁵⁰ We further demonstrated the excellent structural stability of (R-PyEA)Pb₂Br₆ perovskite under room temperature conditions, which facilitates the steady operation of chiral 3D perovskites optoelectronic devices at an ambient temperature (Figure 2f). The relationship between the exciton binding energy and the integrated

photoluminescence intensity at different temperatures can be expressed by the Arrhenius equation

$$I_T = \frac{I_0}{1 + A e^{-E_B/k_B T}}$$

where I_T , I_0 , E_B , and k_B are the integral PL intensity, the integral PL intensity at 0 K, the exciton binding energy, and the Boltzmann constant, respectively. The extracted exciton binding energy of (R-PyEA)Pb₂Br₆ perovskite is 57.3 meV, which is smaller than those of previously reported 2D lead bromide perovskites and larger than those of the traditional 3D lead bromide perovskites (Figure 2g and Table S4).

To achieve a one-step integration of chiral 3D perovskite microwire arrays on the gold electrode substrate, we developed a capillary-bridge assembly technology by manipulating the transport dynamics of fluids (see the schemes in Figure 3a,b). The detailed assembly method is shown in the Experimental Section. First, the precursor solution of chiral 3D perovskite is confined between an asymmetric-wettability topographical template (i.e., lyophilic tops and lyophobic sidewalls of micropillars) and the target Au electrode substrate, forming a sandwich-type assembly system (Figures S9 and S10). Then, with the evaporation of solvent, independent capillary liquid bridges are developed. Furthermore, the site-specific nucleation and the directional growth guarantee the formation of long-range oriented chiral 3D perovskite microwire arrays on

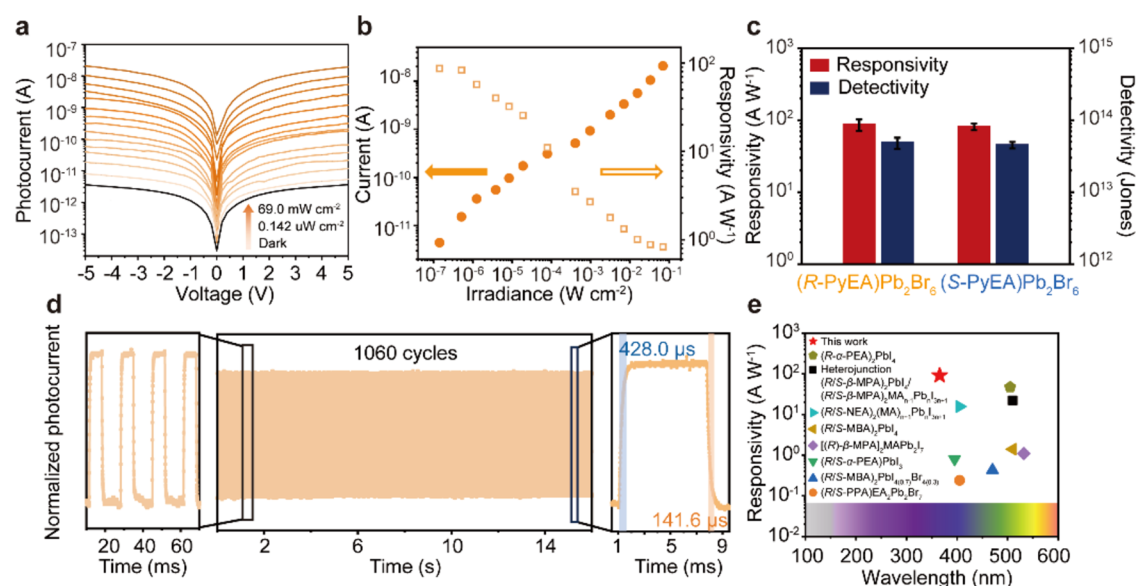


Figure 4. Photodetector performance of chiral 3D perovskite array devices. (a) $(R\text{-PyEA})\text{Pb}_2\text{Br}_6$ perovskite array device under dark and unpolarized 365 nm with different illumination. (b) The irradiance-dependent photocurrents and responsivities of $(R\text{-PyEA})\text{Pb}_2\text{Br}_6$ perovskite array device under unpolarized 365 nm illumination. (c) Statistics of responsivity and detectivity of $(R\text{-PyEA})\text{Pb}_2\text{Br}_6$ and $(S\text{-PyEA})\text{Pb}_2\text{Br}_6$ perovskite array devices. (d) The cyclic stability test of $(R\text{-PyEA})\text{Pb}_2\text{Br}_6$ perovskite array device. (e) Statistical diagram of the responsivity for CPL detection.

the target Au electrode substrate. Figures 3c and S11 present strict alignment, homogeneous size, and precise position of chiral 3D perovskite microwire arrays on the Au electrode substrate.

To further investigate the morphology, crystallinity, and orientation of the chiral 3D perovskite microwire arrays, scanning electron microscopy (SEM), atomic force microscopy (AFM), X-ray Diffraction (XRD), transmission electron microscopy (TEM), and grazing-incidence wide-angle X-ray scattering (GIWAXS) were carried out. SEM images illustrate the smooth surface, sharp edge, and strict alignment of the chiral 3D perovskite microwire arrays (Figures S12 and S13a). In addition, AFM measurement presents a smooth surface with a uniform height of ca. 368.5 nm and a width of ca. 2 μm , proving the high crystallinity without grain boundary of chiral 3D perovskite microwire arrays (Figures 3d and S13b). XRD patterns exhibit a series of periodic diffraction peaks, which can be assigned as (020), (040), and (060) planes, indicating the oriented growth and high crystallinity of $(R\text{-PyEA})\text{Pb}_2\text{Br}_6$ and $(S\text{-PyEA})\text{Pb}_2\text{Br}_6$ perovskite microwire arrays (Figure 3e). The GIWAXS patterns exhibit sharp and discrete diffraction spots, which can be attributed to pure (020)-oriented microwire arrays, corresponding to the XRD results (Figures 3f and S14). TEM images further illustrate a sharp edge and smooth surface of the chiral perovskite microwire. The corresponding selected area electron diffraction (SAED) patterns present sharp diffraction spots, demonstrating excellent crystallinity and a preferential growth direction along [200] (Figures 3g and S15). Furthermore, the Bravais–Friedel–Donnay–Harker (BFDH) morphology calculation results based on the chiral 3D perovskite crystal structure reveal dominant growth direction along the a -axis, which is consistent with the result of SAED patterns, demonstrating the orientational growth and high crystallinity of chiral 3D perovskite microwire arrays (Figures 3h and S16). Moreover, the influence of pressure and solution concentration on regulating the nucleation and growth of molecules has been reported.⁵² Through careful

tuning of the pressure and solution concentration, chiral 3D perovskite microwire arrays with heights ranging from 200 to 800 nm were fabricated (Figure S17).

To further investigate the optical properties of chiral 3D perovskite microwire arrays, ultraviolet–visible (UV–vis) and CD spectra were then measured. $(R\text{-PyEA})\text{Pb}_2\text{Br}_6$ and $(S\text{-PyEA})\text{Pb}_2\text{Br}_6$ perovskite microwire arrays exhibit a similar profile with an exciton resonance centered at 400 nm (Figure 3i). CD spectra further demonstrate the selective CPL absorption properties of the chiral 3D perovskites. As shown in Figure 3j, the $(R\text{-PyEA})\text{Pb}_2\text{Br}_6$ and $(S\text{-PyEA})\text{Pb}_2\text{Br}_6$ perovskite microwire arrays display a significantly opposite CD absorption signal at the same peak position from 200 to 500 nm. The bisignated CD signals are located around the exciton absorption peak of $(R/S\text{-PyEA})\text{Pb}_2\text{Br}_6$, which is attributed to the Cotton effect.²⁰ Compared with the CD absorption signal of chiral 3D perovskites, distinctly different CD absorption peaks of $R/S\text{-PyEA}$ ammonium cations (ranged from 285 to 360 nm) indicate that the CD signals of chiral 3D perovskites originate from the efficient transfer of chirality from organic chiral cations to the inorganic framework (Figure S18).^{14,26,28} Furthermore, the anisotropy factor g_{CD} is calculated as $g_{\text{CD}} = \text{CD}[\text{mdeg}]/32,980 \times A$, where A represents the absorbance of nonpolarized light and CD represents the differential absorbance of right- and left-handed CPL, respectively. The maximum g_{CD} value is approximately 0.0025 for $(R\text{-PyEA})\text{Pb}_2\text{Br}_6$ perovskite microwire arrays (Figure S19).

To evaluate the optoelectronic performance of high-quality chiral 3D perovskite microwire arrays, two-terminal photodetectors were fabricated based on chiral 3D perovskite microwires by the one-step capillary-bridge assembly technology. $(R\text{-PyEA})\text{Pb}_2\text{Br}_6$ and $(S\text{-PyEA})\text{Pb}_2\text{Br}_6$ perovskite microwire arrays present a very low dark current around 10^{-12} A at a bias of 5 V, which should be ascribed to the exceptional crystallinity of perovskite microwires with suppressed defect density (Figures 4a and S22a). Under the unpolarized 365 nm

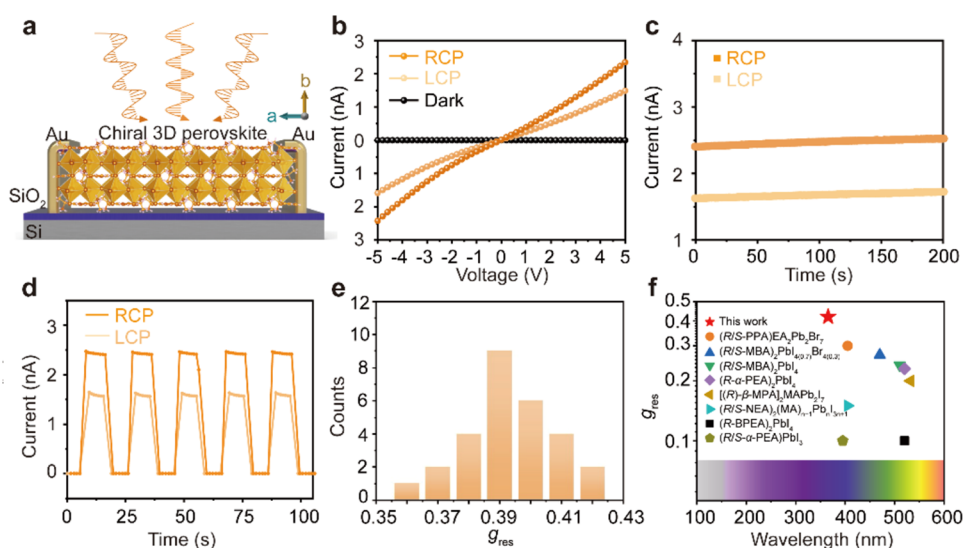


Figure 5. CPL detection performance of chiral 3D perovskite microwire arrays. (a) A schematic diagram of multifunctional photodetectors. (b) The current–voltage (I - V) curves of $(R\text{-PyEA})\text{Pb}_2\text{Br}_6$ perovskite array device under dark, 365 nm RCP, and 365 nm LCP light illumination. (c) The current–time (I - t) curves of $(R\text{-PyEA})\text{Pb}_2\text{Br}_6$ perovskite array device under 365 nm RCP and 365 nm LCP light illumination at 5 V bias. (d) The recyclable RCP-365 and LCP-365 nm response of $(R\text{-PyEA})\text{Pb}_2\text{Br}_6$ perovskite array device at 5 V bias with 69.0 mW cm^{-2} intensity. (e) The statistical g_{res} values of $(R\text{-PyEA})\text{Pb}_2\text{Br}_6$ perovskite array device. (f) Comparison between $(R\text{-PyEA})\text{Pb}_2\text{Br}_6$ perovskite array device and other chiral perovskite CPL detectors that have been reported.

light illumination, the photocurrents show nearly 4 orders of magnitude increased up to 10^{-8} A owing to the efficient photocarrier transport. Responsivity is an important metric to evaluate the performance of photodetectors, which can be determined by $R = (I_{\text{light}} - I_{\text{dark}})/P$, where I_{light} , I_{dark} , and P represent the light current, dark current, and illumination power, respectively. The photocurrents and responsivities of $(R\text{-PyEA})\text{Pb}_2\text{Br}_6$ and $(S\text{-PyEA})\text{Pb}_2\text{Br}_6$ perovskite array devices exhibit positive and negative linear associations (Figures 4b and S22b). The detectivity (D^*) is another important merit of photodetectors, defined as $D^* = (RA^{1/2})/(2qI_{\text{dark}})^{1/2}$, where A represents the effective area and q represents the absolute value of the electron charge. The responsivity and detectivity of $(R\text{-PyEA})\text{Pb}_2\text{Br}_6$ and $(S\text{-PyEA})\text{Pb}_2\text{Br}_6$ perovskite array devices are calculated and shown in Figure 4c. Typically, the detectivity of $(R\text{-PyEA})\text{Pb}_2\text{Br}_6$ perovskite array devices reaches the highest value around 4.84×10^{13} Jones, corresponding to the responsivity of 86.7 A W^{-1} under the irradiance of $0.142 \mu\text{W cm}^{-2}$. To further evaluate the temporal response of array devices, we monitored the rise and decay time, which is defined as the photocurrent increasing from 10 to 90% and decreasing from 90 to 10%, respectively. As shown in Figure 4d, $(R\text{-PyEA})\text{Pb}_2\text{Br}_6$ perovskite array devices exhibit the fastest response speed of $428.0 \mu\text{s}$ for rise and $141.6 \mu\text{s}$ for decay under 69.0 mW cm^{-2} . In addition, the perovskite microwire photodetector shows exceptional operational stability with no degradation of performance after 1060 switching cycles. Compared with single-crystal array devices, thin-film-based devices display lower performance owing to the huge number of defects and traps (Figure S23). To further demonstrate the high photodetection performance of chiral 3D perovskite array devices, we compare the responsivity of single-crystalline perovskite microwire photodetectors to that of the reported chiral perovskite photodetectors (Figure 4e and Table S5). Chiral 3D perovskite array devices exhibit excellent optoelectronic performance, which is the highest responsivity reported for CPL photodetectors based on chiral perovskites. The

superior performance can be attributed to the small intrinsic exciton binding energy and efficient carrier separation and transport in the chiral 3D perovskite single-crystal microwire arrays with pure orientation and eliminated defects.

Highly efficient CPL absorption and the anisotropic crystal structures of $(R\text{-PyEA})\text{Pb}_2\text{Br}_6$ and $(S\text{-PyEA})\text{Pb}_2\text{Br}_6$ microwire arrays enable the detection of both linearly and circularly polarized light (Figure 5a). First, we investigated the circularly polarized photodetection properties of the array devices under right-handed circularly polarized (RCP) and left-handed circularly polarized (LCP) light. The I - V curves of $(R\text{-PyEA})\text{Pb}_2\text{Br}_6$ and $(S\text{-PyEA})\text{Pb}_2\text{Br}_6$ microwire array devices present an obvious unidentical photoresponse under RCP and LCP illumination at 365 nm, confirming the prominent CPL detection capability to distinguish RCP and LCP light (Figures 5b and S24a). In addition, the I - t curves of $(R\text{-PyEA})\text{Pb}_2\text{Br}_6$ perovskite array devices under RCP and LCP light illumination are presented in Figure 5c, which demonstrates the extremely stable CPL detection performance of the chiral 3D perovskite array devices. The temporal response of chiral 3D perovskite array devices under RCP and LCP light illumination further verifies the excellent CPL detection performance (Figures 5d and S24b). To quantify the distinguishability of CPL detection of $(R\text{-PyEA})\text{Pb}_2\text{Br}_6$ perovskite array devices, the anisotropy factor for responsivity (g_{res}) is defined as $g_{\text{res}} = 2(R_L - R_R)/(R_L + R_R)$, where R_L and R_R represent the responsivity under LCP and RCP light illumination, respectively. The statistical g_{res} values of $(R\text{-PyEA})\text{Pb}_2\text{Br}_6$ perovskite array devices are shown in Figure 5e, where the maximum g_{res} value is 0.42, which is calculated under 365 nm light illumination. Compared with the polycrystalline thin-film devices with poor CPL performance, the high g_{res} of chiral 3D perovskite single-crystal array devices arises from their high crystallinity and pure orientation, which significantly promotes the separation and transport of photoinduced spin carriers (Figures S25 and S26). The more effective chirality-induced spin selectivity (CISS) of the chiral 3D perovskite microwire arrays is further demonstrated by the

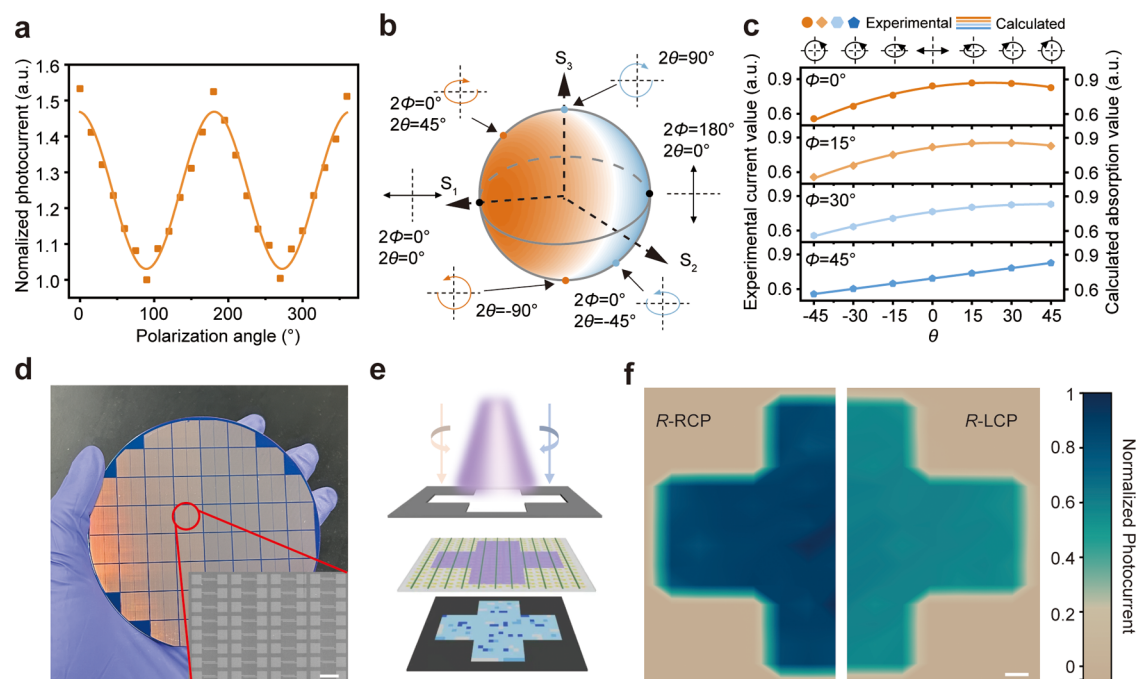


Figure 6. Full-Stokes polarimeter and imaging of chiral 3D perovskite microwire arrays. (a) Angle-dependent photocurrents of the (*R*-PyEA)Pb₂Br₆ perovskite array device at different polarization angles under 365 nm irradiation with 69.0 mW cm⁻² intensity. (b) Poincaré-sphere representation for different polarization states of light. The different colors on the surface of the Poincaré sphere exhibit the theoretical absorption intensity with varying Stokes parameters. (c) Measured (orange solid circles) and calculated (black hollow circles) Stokes parameters for incident light with six different polarization states. The average measurement error is shown in the right plots. (d) Digital photo of microwire arrays fabrication on a 4 in. silicon dioxide wafer. Inset: Magnified microwire arrays. (e) A schematic illustration of the imaging sensing system. (f) Imaging results of the cross-shaped pattern for the (*R*-PyEA)Pb₂Br₆ perovskite array device under RCP and LCP illumination. Scale bars: (d) 100 μm; (f) 200 μm.

magnetic conductive-probe AFM (mCP-AFM) (Figure S27).⁵³ To further highlight the superiority of chiral 3D perovskite CPL photodetectors, we statistically compared the performance of recently reported CPL photodetectors based on low-dimensional perovskites (Figure 5f and Table S6). The statistical g_{res} indicates that our fabricated 3D perovskite CPL photodetectors exhibit better performance.

Then, we analyzed the linearly polarized light detection performance of chiral 3D perovskite microwire arrays. The anisotropic crystal structures of (*R*-PyEA)Pb₂Br₆ and (*S*-PyEA)Pb₂Br₆ also ensure the linearly polarized light absorption of the microwire arrays. The anisotropic optical absorption of chiral 3D perovskite microwires yields anisotropic photocurrents under different linearly polarized light. Figure 6a shows that the photocurrents of (*R*-PyEA)Pb₂Br₆ perovskite devices vary as a function of polarization angle under 365 nm linearly polarized light illumination, exhibiting a clear angularly dependent performance of the devices. The 0° polarization is parallel to the growth direction of the perovskite arrays. As the incident light is rotated from 0 to 180°, the photocurrents and polarization angle exhibit a sinusoidal function variation. The largest linear dichroic ratio of the chiral 3D perovskite array device is about 1.52, which is calculated from the equation $I_{\text{max}}/I_{\text{min}}$. In contrast to single-crystalline microwire arrays, polycrystalline thin-film devices are not sensitive to linearly polarized light owing to the lack of anisotropy (Figures S28 and S29). The excellent performance for linearly polarized light detection benefits from the large optical anisotropy of chiral 3D perovskite microwires.

Given the sensitivity to both linearly and circularly polarized light of chiral 3D perovskite microwires, the full-Stokes polarimeter was further demonstrated. As illustrated in Figures

6b and S30, the normalized calculated absorption coefficient exhibits a clear dependence on the Stokes parameters, where Φ represents the angle between the x -direction and the fast axis of the $\lambda/4$ plate and θ represents the angle between the linearly polarized light and the fast axis of the $\lambda/4$ plate. To validate the full-Stokes polarimeter, we modulated different polarized light by combining a $\lambda/2$ plate and a $\lambda/4$ plate. The polarization states of light can be described by four Stokes parameters (S_0 , S_1 , S_2 , and S_3), where $S_0 = I$, $S_1 = I_h - I_v$, $S_2 = I_{+\pi/4} - I_{-\pi/4}$, and $S_3 = I_R - I_L$.⁵⁴ Here, I is the total intensity; I_h , I_v , $I_{+\pi/4}$, $I_{-\pi/4}$, I_R , and I_L are the intensity of horizontally linearly polarized components, vertically linearly polarized component, linear +45° polarized component, linear -45° polarized component, right-handed circularly polarized component, and left-handed circularly polarized component, respectively. Figure 6c shows the Stokes parameters (S_0 , S_1 , S_2 , and S_3) obtained by a full-Stokes polarimeter and theoretically calculated values. The measured Stokes parameters of chiral 3D perovskite devices under different polarization states are well fitted with the theoretical values. The average measurement errors of S_1 , S_2 , and S_3 are 1.77, 3.18, and 2.02%, respectively, confirming the realization of fully polarized light photodetectors in chiral 3D perovskite microwire arrays.

Considering the excellent performance and large-area integrated manufacturing of chiral 3D perovskite CPL photodetectors, we constructed an image-sensing system for optoelectronic imaging applications. Figure 6d shows large-area chiral 3D perovskite array devices integrated on the Si/SiO₂ wafer, demonstrating the feasibility of wafer-scale integration based on array devices. The SEM image further exhibits the regular alignment of the CPL photodetector. The image-sensing system mainly consists of 16 × 16 pixels (3.584

mm²) CPL photodetector arrays, LED light sources, waveplates, and cross-shaped microwire photomask (Figure 6e). The current density of each pixel is recorded and normalized. Under CPL illumination, pixels in the hollow cross-shaped pattern area show higher current values, while the pixels covered by the photomask show no noticeable difference with a dark current. As shown in Figure 6f, obviously unidentical photoresponse between the left and right regions of the cross-shaped pattern are observed under RCP and LCP illumination, respectively, confirming the excellent distinguishability of CPL for chiral 3D perovskite array devices. Simultaneously, the sharp boundaries of cross-shaped patterns illustrate the high fidelity of microwire perovskite photodetectors in the optoelectronic imaging area. In general, we have realized a low-cost, large-area, and high-fidelity CPL imaging technique, which accelerates the application of CPL detection toward real applications.

CONCLUSIONS

In conclusion, we have pioneered the fabrication of chiral 3D perovskite integrated devices by a one-step capillary-bridge assembly technology. The unprecedented chiral 3D perovskites (R/S-PyEA)Pb₂Br₆ exhibit a smaller exciton binding energy as well as significant CD absorption. Owing to the high crystallinity, strict alignment, and homogeneous size of wafer-scale integrated chiral 3D perovskite microwire arrays, the CPL photodetectors exhibit remarkable performance with a superior responsivity of 86.7 A W⁻¹, a detectivity exceeding 4.84 × 10¹³ Jones, a circular-/linear-polarization anisotropy factor of 0.42/1.52, and large-area high-fidelity imaging with 256 pixels. Based on the circular- and linear-polarization sensitivity of chiral 3D perovskite microwire arrays, the full-Stokes polarimeter was demonstrated. This assembly technology with controllable fluid transport, large-scale patterning, and long-range oriented crystallization provides a promising platform for large-area wafer integration of high-performance chiral spin-optoelectronic devices.

ASSOCIATED CONTENT

Supporting Information

The Supporting Information is available free of charge at <https://pubs.acs.org/doi/10.1021/jacs.4c06822>.

Experimental section, schematic illustrations, crystal structure, Hirshfeld surfaces, 2D-fingerprint plots, TGA measurement, effective masses, DRS spectrum, time-resolved PL decay spectra, optical microscope images, SEM images, AFM images, GIWAXS patterns, TEM images, the BFDH morphology, CD spectra, the g_{res} result, detailed photodetector characteristics, mCP-AFM results, crystallographic information on chiral 3D perovskites, summary of exciton binding energy of perovskites, and summary of performance of CPL photodetectors (PDF)

Accession Codes

CCDC 2333429 and 2333431 contain the supplementary crystallographic data for this paper. These data can be obtained free of charge via www.ccdc.cam.ac.uk/data_request/cif, by emailing data_request@ccdc.cam.ac.uk, or by contacting The Cambridge Crystallographic Data Centre, 12 Union Road, Cambridge CB2 1EZ, U.K.; fax: +44 1223 336033.

AUTHOR INFORMATION

Corresponding Authors

Yingjie Zhao – College of Chemistry, Zhengzhou University, Zhengzhou 450001, P. R. China; Email: zhaoyingjie5@zzu.edu.cn

Guankui Long – School of Materials Science and Engineering, Smart Sensing Interdisciplinary Science Center, Tianjin Key Lab for Rare Earth Materials and Applications, Renewable Energy Conversion and Storage Center (RECAST), National Institute for Advanced Materials, Nankai University, Tianjin 300350, P. R. China; orcid.org/0000-0002-1826-3736; Email: longgk09@nankai.edu.cn

Yuchen Wu – Key Laboratory of Bio-inspired Materials and Interfacial Science, Technical Institute of Physics and Chemistry, Chinese Academy of Sciences, Beijing 100190, P. R. China; School of Future Technology, University of Chinese Academy of Sciences, Beijing 100049, P. R. China; orcid.org/0000-0002-3451-7062; Email: wuyuchen@iccas.ac.cn

Authors

Junli Bai – Key Laboratory of Bio-inspired Materials and Interfacial Science, Technical Institute of Physics and Chemistry, Chinese Academy of Sciences, Beijing 100190, P. R. China; School of Future Technology, University of Chinese Academy of Sciences, Beijing 100049, P. R. China

Hebin Wang – School of Materials Science and Engineering, Smart Sensing Interdisciplinary Science Center, Tianjin Key Lab for Rare Earth Materials and Applications, Renewable Energy Conversion and Storage Center (RECAST), National Institute for Advanced Materials, Nankai University, Tianjin 300350, P. R. China

Jianpeng Ma – Key Laboratory of Bio-inspired Materials and Interfacial Science, Technical Institute of Physics and Chemistry, Chinese Academy of Sciences, Beijing 100190, P. R. China; School of Future Technology, University of Chinese Academy of Sciences, Beijing 100049, P. R. China

Haolin Lu – School of Materials Science and Engineering, Smart Sensing Interdisciplinary Science Center, Tianjin Key Lab for Rare Earth Materials and Applications, Renewable Energy Conversion and Storage Center (RECAST), National Institute for Advanced Materials, Nankai University, Tianjin 300350, P. R. China

Yunxin Zhang – School of Materials Science and Engineering, Smart Sensing Interdisciplinary Science Center, Tianjin Key Lab for Rare Earth Materials and Applications, Renewable Energy Conversion and Storage Center (RECAST), National Institute for Advanced Materials, Nankai University, Tianjin 300350, P. R. China

Sehrish Gull – School of Materials Science and Engineering, Smart Sensing Interdisciplinary Science Center, Tianjin Key Lab for Rare Earth Materials and Applications, Renewable Energy Conversion and Storage Center (RECAST), National Institute for Advanced Materials, Nankai University, Tianjin 300350, P. R. China

Tianjiao Qiao – School of Materials Science and Engineering, Smart Sensing Interdisciplinary Science Center, Tianjin Key Lab for Rare Earth Materials and Applications, Renewable Energy Conversion and Storage Center (RECAST), National Institute for Advanced Materials, Nankai University, Tianjin 300350, P. R. China

Wei Qin – School of Physics, State Key Laboratory of Crystal Materials, Shandong University, Jinan 250100, P. R. China; orcid.org/0000-0003-4579-0061

Yongsheng Chen – The Centre of Nanoscale Science and Technology and State Key Laboratory of Elemento-Organic Chemistry, Frontiers Science Center for New Organic Matter, College of Chemistry, Nankai University, Tianjin 300071, P. R. China; orcid.org/0000-0003-1448-8177

Lei Jiang – Key Laboratory of Bio-inspired Materials and Interfacial Science, Technical Institute of Physics and Chemistry, Chinese Academy of Sciences, Beijing 100190, P. R. China; School of Future Technology, University of Chinese Academy of Sciences, Beijing 100049, P. R. China; orcid.org/0000-0003-4579-728X

Complete contact information is available at:
<https://pubs.acs.org/10.1021/jacs.4c06822>

Author Contributions

[†]J.B. and H.W. contributed equally to this work.

Notes

The authors declare no competing financial interest.

ACKNOWLEDGMENTS

This work was supported by the Ministry of Science and Technology of China (2018YFA0704803), the National Natural Science Foundation of China (52173190, 52303257, 92256202, 12261131500, 52203224, 21988102, and 52103218), the Youth Innovation Promotion Association CAS (2018034), the China Postdoctoral Science Foundation (2023TQ0300 and 2023M743171), the Postdoctoral Fellowship Program of CPSF (GZB20230666), and the Key Research & Development and Promotion of Special Project (Scientific Problem Tackling) of Henan Province (242102211090). The authors would like to express their thanks to the Nanofab Lab of the National Center for Nanoscience and Technology for its assistance in the evaporation of metal electrodes. A portion of this work is based on the data obtained at BSRF-1W1A. The authors gratefully acknowledge the cooperation of Dr. Yu Chen at the BSRF-1W1A beamline. All of the theoretical calculations were performed at the National Supercomputer Center in Guangzhou.

REFERENCES

- (1) Stranks, S. D.; Eperon, G. E.; Grancini, G.; Menelaou, C.; Alcocer, M. J. P.; Leijtens, T.; Herz, L. M.; Petrozza, A.; Snaith, H. J. Electron-hole diffusion lengths exceeding 1 micrometer in an organometal trihalide perovskite absorber. *Science* **2013**, *342* (6156), 341–344.
- (2) Abdi-Jalebi, M.; Andaji-Garmaroudi, Z.; Cacovich, S.; Stavrakas, C.; Philippe, B.; Richter, J. M.; Alsari, M.; Booker, E. P.; Hutter, E. M.; Pearson, A. J.; Lilliu, S.; Savenije, T. J.; Rensmo, H.; Divitini, G.; Ducati, C.; Friend, R. H.; Stranks, S. D. Maximizing and stabilizing luminescence from halide perovskites with potassium passivation. *Nature* **2018**, *555* (7697), 497–501.
- (3) Li, X.; Bi, D.; Yi, C.; Décoppet, J.-D.; Luo, J.; Zakeeruddin, S. M.; Hagfeldt, A.; Grätzel, M. A vacuum flash-assisted solution process for high-efficiency large-area perovskite solar cells. *Science* **2016**, *353* (6294), 58–62.
- (4) Kim, Y.-H.; Kim, S.; Kakekhani, A.; Park, J.; Park, J.; Lee, Y.-H.; Xu, H.; Nagane, S.; Wexler, R. B.; Kim, D.-H.; Jo, S. H.; Martínez-Sarti, L.; Tan, P.; Sadhanala, A.; Park, G.-S.; Kim, Y.-W.; Hu, B.; Bolink, H. J.; Yoo, S.; Friend, R. H.; Rappe, A. M.; Lee, T.-W. Comprehensive defect suppression in perovskite nanocrystals for

high-efficiency light-emitting diodes. *Nat. Photonics* **2021**, *15* (2), 148–155.

(5) Liu, X.-K.; Xu, W.; Bai, S.; Jin, Y.; Wang, J.; Friend, R. H.; Gao, F. Metal halide perovskites for light-emitting diodes. *Nat. Mater.* **2021**, *20* (1), 10–21.

(6) Lin, K.; Xing, J.; Quan, L. N.; de Arquer, F. P. G.; Gong, X.; Lu, J.; Xie, L.; Zhao, W.; Zhang, D.; Yan, C.; Li, W.; Liu, X.; Lu, Y.; Kirman, J.; Sargent, E. H.; Xiong, Q.; Wei, Z. Perovskite light-emitting diodes with external quantum efficiency exceeding 20 per-cent. *Nature* **2018**, *562* (7726), 245–248.

(7) Feng, J.; Gong, C.; Gao, H.; Wen, W.; Gong, Y.; Jiang, X.; Zhang, B.; Wu, Y.; Wu, Y.; Fu, H.; Jiang, L.; Zhang, X. Single-crystalline layered metal-halide perovskite nanowires for ultrasensitive photodetectors. *Nat. Electron.* **2018**, *1* (7), 404–410.

(8) Deng, W.; Huang, L.; Xu, X.; Zhang, X.; Jin, X.; Lee, S.-T.; Jie, J. Ultrahigh-responsivity photodetectors from perovskite nanowire arrays for sequentially tunable spectral measurement. *Nano Lett.* **2017**, *17* (4), 2482–2489.

(9) Leng, K.; Abdelwahab, I.; Verzhbitskiy, I.; Telychko, M.; Chu, L.; Fu, W.; Chi, X.; Guo, N.; Chen, Z.; Chen, Z.; Zhang, C.; Xu, Q.-H.; Lu, J.; Chhowalla, M.; Eda, G.; Loh, K. P. Molecularly thin two-dimensional hybrid perovskites with tunable optoelectronic properties due to reversible surface relaxation. *Nat. Mater.* **2018**, *17* (10), 908–914.

(10) García de Arquer, F. P.; Armin, A.; Meredith, P.; Sargent, E. H. Solution-processed semiconductors for next-generation photodetectors. *Nat. Rev. Mater.* **2017**, *2* (3), 16100.

(11) Dong, H.; Zhang, C.; Liu, X.; Yao, J.; Zhao, Y. S. Materials chemistry and engineering in metal halide perovskite lasers. *Chem. Soc. Rev.* **2020**, *49* (3), 951–982.

(12) Moon, J.; Mehta, Y.; Gundogdu, K.; So, F.; Gu, Q. Metal-halide perovskite lasers: cavity formation and emission characteristics. *Adv. Mater.* **2024**, *36*, No. 2211284.

(13) Ishii, A.; Miyasaka, T. Direct detection of circular polarized light in helical 1D perovskite-based photodiode. *Sci. Adv.* **2020**, *6* (46), No. eabd3274.

(14) Niu, X.; Zeng, Z.; Wang, Z.; Lu, H.; Sun, B.; Zhang, H.-L.; Chen, Y.; Du, Y.; Long, G. The first chiral cerium halide towards circularly-polarized luminescence in the UV region. *Sci. China Chem.* **2024**, *67*, 1961–1968, DOI: 10.1007/s11426-024-1946-7.

(15) Wang, H.; Li, J.; Lu, H.; Gull, S.; Shao, T.; Zhang, Y.; He, T.; Chen, Y.; He, T.; Long, G. Chiral hybrid germanium(II) halide with strong nonlinear chiroptical properties. *Angew. Chem., Int. Ed.* **2023**, *62* (41), No. e202309600, DOI: 10.1002/anie.202309600.

(16) Fu, D.; Xin, J.; He, Y.; Wu, S.; Zhang, X.; Zhang, X.-M.; Luo, J. Chirality-dependent second-order nonlinear optical effect in 1D organic-inorganic hybrid perovskite bulk single crystal. *Angew. Chem., Int. Ed.* **2021**, *60* (36), 20021–20026.

(17) Hu, Y.; Florio, F.; Chen, Z.; Phelan, W. A.; Siegler, M. A.; Zhou, Z.; Guo, Y.; Hawks, R.; Jiang, J.; Feng, J.; Zhang, L.; Wang, B.; Wang, Y.; Gall, D.; Palermo, E. F.; Lu, Z.; Sun, X.; Lu, T.-M.; Zhou, H.; Ren, Y.; Wertz, E.; Sundararaman, R.; Shi, J. A chiral switchable photovoltaic ferroelectric 1D perovskite. *Sci. Adv.* **2020**, *6* (9), No. eaay4213.

(18) Shi, C.; Ye, L.; Gong, Z.-X.; Ma, J.-J.; Wang, Q.-W.; Jiang, J.-Y.; Hua, M.-M.; Wang, C.-F.; Yu, H.; Zhang, Y.; Ye, H.-Y. Two-dimensional organic-inorganic hybrid rare-earth double perovskite ferroelectrics. *J. Am. Chem. Soc.* **2020**, *142* (1), 545–551.

(19) Ma, S.; Jung, Y.-K.; Ahn, J.; Kyhm, J.; Tan, J.; Lee, H.; Jang, G.; Lee, C. U.; Walsh, A.; Moon, J. Elucidating the origin of chiroptical activity in chiral 2D perovskites through nano-confined growth. *Nat. Commun.* **2022**, *13* (1), No. 3259.

(20) Long, G.; Jiang, C.; Sabatini, R.; Yang, Z.; Wei, M.; Quan, L. N.; Liang, Q.; Rasmita, A.; Askerka, M.; Walters, G.; Gong, X.; Xing, J.; Wen, X.; Quintero-Bermudez, R.; Yuan, H.; Xing, G.; Wang, X. R.; Song, D.; Voznyy, O.; Zhang, M.; Hoogland, S.; Gao, W.; Xiong, Q.; Sargent, E. H. Spin control in reduced-dimensional chiral perovskites. *Nat. Photonics* **2018**, *12* (9), 528–533.

- (21) Liu, Z.; Zhang, C.; Liu, X.; Ren, A.; Zhou, Z.; Qiao, C.; Guan, Y.; Fan, Y.; Hu, F.; Zhao, Y. S. Chiral hybrid perovskite single-crystal nanowire arrays for high-performance circularly polarized light detection. *Adv. Sci.* **2021**, *8* (21), No. 2102065.
- (22) Liu, T.; Shi, W.; Tang, W.; Liu, Z.; Schroeder, B. C.; Fenwick, O.; Fuchter, M. J. High responsivity circular polarized light detectors based on quasi two-dimensional chiral perovskite films. *ACS Nano* **2022**, *16* (2), 2682–2689.
- (23) Zhao, J.; Zhao, Y.; Guo, Y.; Zhan, X.; Feng, J.; Geng, Y.; Yuan, M.; Fan, X.; Gao, H.; Jiang, L.; Yan, Y.; Wu, Y. Layered metal-halide perovskite single-crystalline microwire arrays for anisotropic nonlinear optics. *Adv. Funct. Mater.* **2021**, *31* (48), No. 2105855.
- (24) Liu, S.; Heindl, M. W.; Fehn, N.; Caicedo-Dávila, S.; Eyre, L.; Kronawitter, S. M.; Zerhoch, J.; Bodnar, S.; Shcherbakov, A.; Stadlbauer, A.; Kieslich, G.; Sharp, I. D.; Egger, D. A.; Kartouzian, A.; Deschler, F. Optically induced long-lived chirality memory in the color-tunable chiral lead-free semiconductor (R)/(S)-CHEA₄Bi₂Br_xI_{10-x} (x = 0–10). *J. Am. Chem. Soc.* **2022**, *144* (31), 14079–14089.
- (25) Wang, Q.; Zhu, H.; Tan, Y.; Hao, J.; Ye, T.; Tang, H.; Wang, Z.; Ma, J.; Sun, J.; Zhang, T.; Zheng, F.; Zhang, W.; Choi, A. H. W.; Choy, W. C. H.; Wu, D.; Sun, X. W.; Wang, K. Spin quantum dot light-emitting diodes enabled by two-dimensional chiral perovskite with spin-dependent carrier transport. *Adv. Mater.* **2023**, *36* (5), No. e2305604, DOI: 10.1002/adma.202305604.
- (26) Chen, C.; Gao, L.; Gao, W.; Ge, C.; Du, X.; Li, Z.; Yang, Y.; Niu, G.; Tang, J. Circularly polarized light detection using chiral hybrid perovskite. *Nat. Commun.* **2019**, *10* (1), No. 1927.
- (27) Zhao, Y.; Qiu, Y.; Feng, J.; Zhao, J.; Chen, G.; Gao, H.; Zhao, Y.; Jiang, L.; Wu, Y. Chiral 2D-perovskite nanowires for Stokes photodetectors. *J. Am. Chem. Soc.* **2021**, *143* (22), 8437–8445.
- (28) Wang, L.; Xue, Y.; Cui, M.; Huang, Y.; Xu, H.; Qin, C.; Yang, J.; Dai, H.; Yuan, M. A Chiral reduced-dimension perovskite for an efficient flexible circularly polarized light photodetector. *Angew. Chem., Int. Ed.* **2020**, *59* (16), 6442–6450.
- (29) Peng, Y.; Liu, X.; Li, L.; Yao, Y.; Ye, H.; Shang, X.; Chen, X.; Luo, J. Realization of vis-NIR dual-modal circularly polarized light detection in chiral perovskite bulk crystals. *J. Am. Chem. Soc.* **2021**, *143* (35), 14077–14082.
- (30) Guan, Q.; Zhu, T.; Zhu, Z.-K.; Ye, H.; You, S.; Xu, P.; Wu, J.; Niu, X.; Zhang, C.; Liu, X.; Luo, J. Unprecedented Chiral three-dimensional hybrid organic-inorganic Perovskitoids. *Angew. Chem., Int. Ed.* **2023**, *62* (32), No. e202307034.
- (31) Sheikh, T.; Maqbool, S.; Mandal, P.; Nag, A. Introducing intermolecular cation- π interactions for water-stable low dimensional hybrid lead halide perovskites. *Angew. Chem., Int. Ed.* **2021**, *60* (33), 18265–18271.
- (32) Long, G.; Zhou, Y.; Zhang, M.; Sabatini, R.; Rasmita, A.; Huang, L.; Lakhwani, G.; Gao, W. Theoretical prediction of chiral 3D hybrid organic-inorganic perovskites. *Adv. Mater.* **2019**, *31* (17), No. 1807628.
- (33) Kim, M.; Kim, G.-H.; Lee, T. K.; Choi, I. W.; Choi, H. W.; Jo, Y.; Yoon, Y. J.; Kim, J. W.; Lee, J.; Huh, D.; Lee, H.; Kwak, S. K.; Kim, J. Y.; Kim, D. S. Methylammonium chloride induces intermediate phase stabilization for efficient perovskite solar cells. *Joule* **2019**, *3* (9), 2179–2192.
- (34) Bi, D.; Yi, C.; Luo, J.; Décoppet, J.-D.; Zhang, F.; Zakeeruddin, S. M.; Li, X.; Hagfeldt, A.; Grätzel, M. Polymer-templated nucleation and crystal growth of perovskite films for solar cells with efficiency greater than 21%. *Nat. Energy* **2016**, *1* (10), 16142.
- (35) Nie, W.; Tsai, H.; Asadpour, R.; Blancon, J.-C.; Neukirch, A. J.; Gupta, G.; Crochet, J. J.; Chhowalla, M.; Tretiak, S.; Alam, M. A.; Wang, H.-L.; Mohite, A. D. High-efficiency solution-processed perovskite solar cells with millimeter-scale grains. *Science* **2015**, *347* (6221), 522–525.
- (36) Jeon, N. J.; Noh, J. H.; Yang, W. S.; Kim, Y. C.; Ryu, S.; Seo, J.; Seok, S. I. Compositional engineering of perovskite materials for high-performance solar cells. *Nature* **2015**, *517* (7535), 476–480.
- (37) Jeon, N. J.; Noh, J. H.; Kim, Y. C.; Yang, W. S.; Ryu, S.; Seok, S. I. Solvent engineering for high-performance inorganic-organic hybrid perovskite solar cells. *Nat. Mater.* **2014**, *13* (9), 897–903.
- (38) Cao, J.; Wu, B.; Chen, R.; Wu, Y.; Hui, Y.; Mao, B.-W.; Zheng, N. Efficient, hysteresis-free, and stable perovskite solar cells with ZnO as electron-transport layer: effect of surface passivation. *Adv. Mater.* **2018**, *30* (11), No. 1705596.
- (39) Yao, F.; Peng, J.; Li, R.; Li, W.; Gui, P.; Li, B.; Liu, C.; Tao, C.; Lin, Q.; Fang, G. Room-temperature liquid diffused separation induced crystallization for high-quality perovskite single crystals. *Nat. Commun.* **2020**, *11* (1), No. 1194.
- (40) Ma, J.; Fang, C.; Liang, L.; Wang, H.; Li, D. Full-Stokes polarimeter based on chiral perovskites with chirality and large optical anisotropy. *Small* **2021**, *17* (47), No. 2103855.
- (41) Zhao, Y.; Zhou, Z.; Liu, X.; Ren, A.; Ji, S.; Guan, Y.; Liu, Z.; Liu, H.; Li, P.; Hu, F.; Zhao, Y. S. Chiral 2D/quasi-2D perovskite heterojunction nanowire arrays for high-performance full-Stokes polarization detection. *Adv. Opt. Mater.* **2023**, *11* (19), No. 2301239.
- (42) Gu, Z.; Zhao, Y.; Zhang, Y.; Huang, Z.; Zhou, Z.; Wang, K.; Li, L.; Zhao, Y. S.; Xu, Q.; Song, Y. Ion aggregation-induced crystallization strategy for printing morphology-controllable perovskite single-crystal arrays and integrated devices. *Chem. Mater.* **2023**, *35* (13), 5127–5134.
- (43) Umeyama, D.; Leppert, L.; Connor, B. A.; Manupil, M. A.; Neaton, J. B.; Karunadasa, H. I. Expanded analogs of three-dimensional lead-halide hybrid perovskites. *Angew. Chem., Int. Ed.* **2020**, *59* (43), 19087–19094.
- (44) Chen, W.; Chen, A.; Zhang, R.; Zeng, J.; Zhang, L.; Gu, M.; Wang, C.; Huang, M.; Guo, Y.; Duan, H.; Hu, C.; Shen, W.; Niu, B.; Watanabe, K.; Taniguchi, T.; Zhang, J.; Li, J.; Cai, X.; Liu, G. Strong in-plane optoelectronic anisotropy and polarization sensitivity in low-symmetry 2D violet phosphorus. *Nano Lett.* **2023**, *23* (23), 10821–10831.
- (45) Stoumpos, C. C.; Kanatzidis, M. G. Halide perovskites: poor man's high-performance semiconductors. *Adv. Mater.* **2016**, *28* (28), 5778–5793.
- (46) Zhang, L.; Su, T.; Li, M.; Jia, F.; Hu, S.; Zhang, P.; Ren, W. Accurate band gap prediction based on an interpretable Δ -machine learning. *Mater. Today Commun.* **2022**, *33*, No. 104630.
- (47) Huang, J.; Yuan, Y.; Shao, Y.; Yan, Y. Understanding the physical properties of hybrid perovskites for photovoltaic applications. *Nat. Rev. Mater.* **2017**, *2* (7), 17042.
- (48) Varshni, Y. P. Temperature dependence of the energy gap in semiconductors. *Physica* **1967**, *34* (1), 149–154.
- (49) Jana, M. K.; Song, R.; Liu, H.; Khanal, D. R.; Janke, S. M.; Zhao, R.; Liu, C.; Vally Vardeny, Z.; Blum, V.; Mitzi, D. B. Organic-to-inorganic structural chirality transfer in a 2D hybrid perovskite and impact on Rashba-Dresselhaus spin-orbit coupling. *Nat. Commun.* **2020**, *11* (1), No. 4699.
- (50) Wright, A. D.; Verdi, C.; Milot, R. L.; Eperon, G. E.; Pérez-Osorio, M. A.; Snaith, H. J.; Giustino, F.; Johnston, M. B.; Herz, L. M. Electron-phonon coupling in hybrid lead halide perovskites. *Nat. Commun.* **2016**, *7* (1), No. 11755.
- (51) Sebastian, M.; Peters, J. A.; Stoumpos, C. C.; Im, J.; Kostina, S. S.; Liu, Z.; Kanatzidis, M. G.; Freeman, A. J.; Wessels, B. W. Excitonic emissions and above-band-gap luminescence in the single-crystal perovskite semiconductors CsPbBr₃ and CsPbCl₃. *Phys. Rev. B* **2015**, *92* (23), No. 235210.
- (52) Gao, H.; Qiu, Y.; Feng, J.; Li, S.; Wang, H.; Zhao, Y.; Wei, X.; Jiang, X.; Su, Y.; Wu, Y.; Jiang, L. Nano-confined crystallization of organic ultrathin nanostructure arrays with programmable geometries. *Nat. Commun.* **2019**, *10* (1), No. 3912.
- (53) Lu, H.; Wang, J.; Xiao, C.; Pan, X.; Chen, X.; Brunecky, R.; Berry, J. J.; Zhu, K.; Beard, M. C.; Vardeny, Z. V. Spin-dependent charge transport through 2D chiral hybrid lead-iodide perovskites. *Sci. Adv.* **2019**, *5* (12), No. eaay0571.
- (54) Schaefer, B.; Collett, E.; Smyth, R.; Barrett, D.; Fraher, B. Measuring the Stokes polarization parameters. *Am. J. Phys.* **2007**, *75* (2), 163–168.